Feasibility of embedded distributed optical fibre sensors in thermoplastic composite braided beam structure

Yiding Liu[a,b,*],Anubhav Singh[a], Yifei Yu[a], Remy Guillaume[a], Alastair E.Barnett[c], Steve K.Barbour[c], Darren J. Hughes[a,*]

[a] *WMG, University of Warwick, Coventry, CV4 7AL, UK*

[b] *School of Physics, Engineering and Computer Science, University of Hertfordshire, Hatfield, Hertfordshire AL10 9AB, UK*

[c] *Composite Braiding Limited, Derby, DE24 9FU, UK*

[*] *Corresponding author. Email address: y.liu@herts.ac.uk;*

Abstract

In this paper, consolidation monitoring and structural health monitoring (SHM) of a braided thermoplastic composite beam was performed using a distributed optical fibre sensor (DOFS). The DOFS was manually embedded into the braided preform before melt processing. The real-time strain and temperature data obtained during consolidation and cooling segments were correlated with phase transitions in the thermoplastic matrix. Post consolidation, the quality of the embedded DOFS was investigated using a micro-CT to reveal defects such as waviness and misorientation due to the crude nature of the adopted embedding technique. The manufactured beam was then subjected to repeated loading-unloading cycles in a flexure test. The strain developments along the embedded optical fibre length were comparable with the measurements from Digital Image Correlation (DIC), and further correlated with the post damage observations. Despite the crude method of embedding the optical fibre, the monitored data was useful for consolidation monitoring as well as SHM. This proved that DOFS could be embedded into composite structures without adding no cost, time and complexity thus making them feasible for industrial applications.

Keywords: Distributed Optical Fibre Sensor (DOFS); Braided composites; Consolidation monitoring; Structural Health Monitoring (SHM); Micro-CT.

1 Introduction

Fibre-reinforced polymer composites remain at the heart of future plans for lightweight structures in sectors as diverse as aerospace, road/rail-based passenger vehicles and offshore power generation. This is due to their high strength-to-weight ratio, as well as design flexibility and corrosion resistance and durability. A significant number of composite manufacturing processes have been developed during the last 40 years including compression moulding, vacuum/bag/autoclave moulding, resin transfer mounding (RTM), filament winding etc. [1], depending on the material, design and the application.

A critical disadvantage of composites is the occurrence of barely visible damage (BVD) [2–4]. Given the complex multi-layered structure of composites, these defects are extremely difficult to detect, but bear the potential to significantly compromise the structural properties. Consequently, designers are compelled to use conservative factors of safety, which restrict the maximum exploitation of the unique properties possessed by composites. In terms of structural inspections, current industry practice involves scheduled maintenance that involves routine but rigorous checks for such hidden damages. Such inspections often prove trivial but require the structures to be taken out of service, resulting in significant loss of revenue. In the aerospace industry, inspection accounts for 27% of the total lifecycle cost of an aircraft [5]. Therefore, there have been significant efforts aimed at replacing scheduled maintenance with condition-based maintenance [6], enabled by active Structural Health Monitoring (SHM) technologies.

A preferable approach which has received some attention is in-situ internal health monitoring which typically relies on multiple sensors installed across the entire structure that provide regular status of the structure's safety. However, typically available sensor technologies provide point-based strain/temperature measurements and large-scale monitoring would add significant cost, complexity and mass. The embedding of optical fibre sensors does not have a significant impact on the mechanical properties of the structures when used for in-situ composite monitoring [7–9]. This has been demonstrated with the traditional fibre optic sensor, i.e., Fibre Bragg Gratings (FBG), which are used to conduct measurements at single or discrete points along the length of an optical fibre. A more recent technology, i.e., Distributed Optical Fibre Sensors (DOFS) provide further advantage by eliminating the need to etch individual gratings into a fibre, hence enabling a continuous measurement along the optical fibre at a much lower cost. Several authors have investigated the potential of embedding different types of optical fibres into composite structures for real-time structural health monitoring to detect cracks, delamination or debonding by relating the distortion spectrum to the specific defect and damaging mechanism. Moreover, a few notable studies have also investigated the potential of optical fibres for monitoring composites during the manufacturing process (curing for thermosets; melting/reconsolidation for thermoplastics) and capture the phase transitions at material level. Table 1 summarises such investigations from the existing academic literature.

Table 1 The usage of optical fibre technique in the structural health monitoring and process monitoring of composites reported in the literature

Reference	Materials	Type of optical fibre	Structural health monitoring	Process monitoring
Rufai et al. [9,10]	Woven E-glass fibre fabric and epoxy resin composite plate by Vacuum-Assisted Resin Infusion Moulding (VARIM)	Micro-braided DOFS	Four-point bending test	Residual strain measurement in the longitudinal and transverse directions
Mulle et al. [11]	Glass-fibre-reinforced polypropylene (GFRP)	FBG	—	Strain variations related to physical change of the laminate related with cooling rate and coefficients of thermal expansion (CTE)
Sorensen et al. [12]	Carbon fibre-reinforced polyphenylene sulphide (AS4/PPS) thermoplastic composite	FBG		Strain development responded to changes in material state, especially the glass-rubber transition and solid–liquid transition
Arhant et al. [13]	Unidirectional C/PA6 thermoplastic panel	a shamrock shaped DOFS placement		Strain measurement of along all the principal directions (0, ±45 and 90°)
Huang C et al. [14]	Carbon fibre/Epoxy by autoclave	Brillouin-scattering-based DOFS		Residual strain measurement
De Baere et al. [15]	Carbon fabric-reinforced PPS	FBG	Fatigue load measurement and the FBG showed the capability of surviving over half a million loading cycles without debonding	
Califano et al. [16]	Unidirectional carbon fibre fabric	Polyimide-coated silica glass DOFS	Integrate with machine learning methods to associate to damage patterns	
Sawicki et al. [17]	Ultra-High Performance Fibre Reinforced Cemetitious (UHPFRC)	DOFS	Four-point bending test of a UHPFRC beam to precisely detect and localize the microcracks in the elastic phase	
Lau et al. [18]	Composite-strengthened concrete	FBG	Strain measurement when the structure is subjected to debond or micro-crack failure	

Ryu et al. [19]	CFRP	FEG	Instrumented a wing box using 24 FBG sensors and an interrogator based on a wavelength-swept fibre laser (WSFL) demonstrating the capability to monitor in real-time the buckling behaviour of a wing box.	
Minakuchi et al. [20]	CFRP panel	DOFS	Estimate effectively the the damage which occurred during impact tests	Estimate effectively the residual strains after manufacturing

To the best of authors' knowledge, these published works applied different kinds of optical fibres in flat thermoset/thermoplastic coupons or panels made by tradition manufacturing tools. Composites manufactured via braiding have attracted significant interest in a variety of industries such as automotive, aerospace and battery enclosures for advanced electric vertical take-off and landing vehicles [21], due to the advantages that the shape of the resulting braiding preforms could be matched closely with that of the finally required components, thus reducing material wastage [22]. Moreover, the interlacement of the fibres imparts superior resistance to damage propagation compared to traditional laminates [23].

Another noteworthy observation from the reviewed papers is the use of localisation mechanisms, for instance, epoxy adhesives in [9], to ensure consistent and controlled orientation of the optical fibres within the composite's structures. This is because the shift between the yarns and warp during the laying-down of optical fibre is difficult to control. A few investigations presented the use of advanced non-destructive techniques such as micro-CT [24] to interpret the position profile or quality control of a FBG when inserted into a carbon polyphenyl sulphide (PPS) woven fabric plates. While controlled orientation of the optical fibres is deemed important for understanding material behaviour, the practices implemented to maintain orientation may reduce the practical feasibility of these systems by adding cost and/or time to the manufacturing process, especially for woven and braided materials. Therefore, it is important to question the importance of orientation, particularly for SHM, as the relative change in the measured signal irrespective of orientation could prove sufficient for the intended purpose.

Considering the research gaps above, this paper presents an investigation of process as well structural health monitoring for a tubular braided thermoplastic composite beam using an embedded DOFS system. Compared to previous studies, the DOFS was embedded during the manufacturing of a braided GFRP beam with relatively less control for ensuring minimum disruption of the process. Following the manufacturing process, the position check and quality control of the embedded DOFS were further interpreted by a micro-CT investigation. Strain data was continuously acquired from the DOFS and processed to perform consolidation monitoring during the moulding process. Furthermore, structural health monitoring during mechanical loading cycles applied to the manufactured part. The results of the study indicate if the DOFS system is robust enough to replicate its ability to identify damage initiation without controlled orientation

2 Rayleigh scattering based DOFS

Herein we examine Rayleigh scattering based optical fibre sensors due to their high chemical stability and small diameters. Such fibres were embedded to the anode electrode of a prototype pouch cell to monitor the distributed strain and temperature in real-time during various operating conditions.

When an electromagnetic wave is launched into an optical fibre, the light will be redistributed by Rayleigh scattering [25]. If the local changes in temperature and strain are relayed to the optical fibres,

the scattered signal in the fibre will be modulated by these physical parameters. As a result, by measuring changes in the modulated signal, it is possible to quantify local physical variables of temperature and strain. The desired features of Rayleigh scattering based fibre sensing technique allows distributed measurements with millimetre-scale spatial resolution and high measurement accuracy, making it a suitable solution for in-situ applications.

Coherent Optical Frequency Domain Reflectometry (C-OFDR), a type of Rayleigh scattering based DOFS, is performed to monitor distributed strain and temperature of the anode electrode. C-OFDR was selected due to its high spatial resolution (2.6 mm) measurement capability. The configuration consists of a main interferometer and an auxiliary interferometer, as shown in supplementary Figure 1. The main interferometer contains two optical couplers (OC1 and OC2), an optical circulator (CIR), two polarization controllers (PC1 and PC2), a fibre under test (FUT) and a polarization beam splitter (PBS). The auxiliary interferometer includes two optical couplers (OC3 and OC4). The optical frequency of the output laser from the tuneable laser source (TLS) is tuned in time, the laser splits into two arms after passing through the OC0. Then the frequency tuning laser launched into the main interferometer splits into two portions at OC1: one (light a) enters the CIR, the PC1 and the FUT, the reference light (light b) enters the PC2. The spontaneous Rayleigh backscattering light in the FUT interferes with light b at the OC2. The interference light transmits to the PBS and then splits into two orthogonal polarization components (P and S). P and S are detected by the photo detectors (PDs) and stored by the data acquisition card (DAQ). In this way, polarization has no effect on the value of Rayleigh backscattering amplitude. Meanwhile, the laser launched into the auxiliary interferometer splits into light c and light d, an interference between them occurs at the OC4, the interference light is employed as a trigger signal to mitigate the tuning nonlinearity.

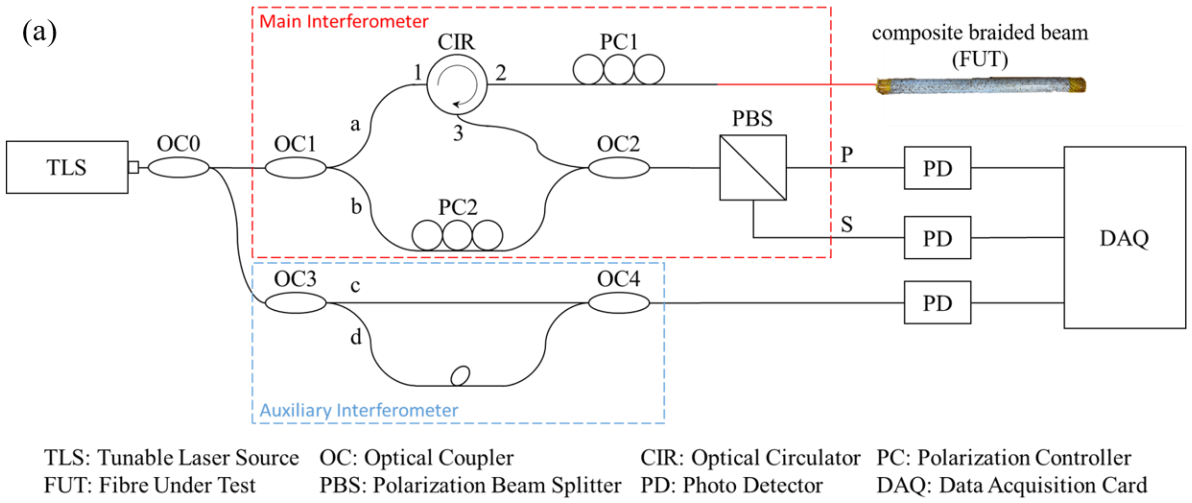

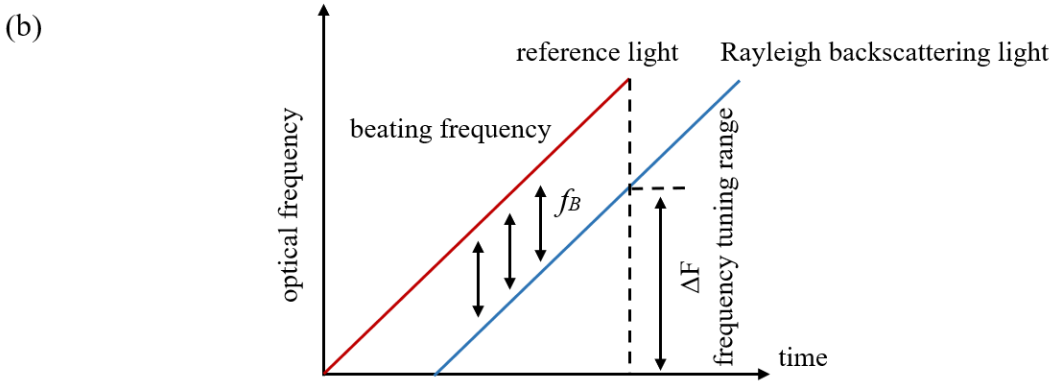

Figure 1: (a) Configuration of a Coherent Optical Frequency Domain Reflectometry (C-OFDR) system. (b) Interference between Rayleigh backscattering light and reference light.

By analysing the interference signal of the main interferometer, it can be found that a specific frequency f_B, named as the beat frequency, directly corresponds to a specific position (z) along the FUT, as indicated in Figure 1(b). The spatial resolution Δz can be given as

$$\Delta z = \frac{c}{2n_g \Delta F} \tag{1}$$

where c is the speed of light in space, n_g is the group refractive index, ΔF is the frequency tuning range of the TLS. In known conditions, a stable and unique fingerprint Rayleigh backscattered spectrum (RBS) is acquired. The local RBS shifts in frequency when a variation in the environmental conditions occurs. The cross-correlation of the measurement RBS and the fingerprint RBS determines the local spectral shift $\Delta\nu$, which can reveal local information (e.g. temperature and strain) along the whole fibre by using proper calibration constants. A change in temperature or strain from the baseline condition results in a frequency shift in the spectrum of light scattered in the fibre. Changes in the local period of Rayleigh scattering cause temporal and spectral shifts in the locally reflected spectrum, which can be scaled to form a distributed sensor. The strain response arises due to both the physical elongation and

compression of the sensor, and the change in fibre index due to photoelastic effects [26]. The thermal response arises due to the inherent thermal expansion of the fibre material and the temperature dependence of the refractive index [26].

The physical length and refraction index of the fibre are intrinsically sensitive to the measurement of both temperature and strain; therefore, the bare fibre sensor is used as the ε-DOFS. The ε-DOFS measures both strain and temperature simultaneously. The resultant measurement is solely a function of variations in temperature. As a result, this fibre is used as *T*-DOFS. The *T*-DOFS measures temperature only. Therefore, in order to capture distributed strain and temperature information respectively, a pair of ε-DOFS and *T*-DOFS were placed parallel and side by side to the subject under test, followed by temperature compensation of strain calibration.

The shift in the spectrum of light scattered in the ε-DOFS in response to strain and temperature is analogous to a shift in the spectral shift, $\Delta\nu_{\varepsilon-DFOS}$:

$$-\frac{\Delta\nu_{\varepsilon-DFOS}}{\nu} = K_T\Delta T_{measured} + K_\varepsilon\varepsilon_{measured} \quad (2)$$

Where ν is the mean optical frequency, K_T and K_ε the temperature and strain calibration constants, $\Delta T_{measured}$ and $\varepsilon_{measured}$ are the measured temperature change and strain.

This thermal response arises due to the inherent thermal expansion of the fibre material and the temperature dependence of the refractive index. In the absence of any mechanical strain, the frequency shift, $\Delta\nu_{T-DFOS}$, due to temperature change ΔT is defined as:

$$-\frac{\Delta\nu_{T-DFOS}}{\nu} = K_T\Delta T_{measured} \quad (3)$$

The default values for these constants are set at common values for germanosilicate core fibres: K_T = 6.45x10^{-6} °C^{-1} and K_ε = 0.780 [27,28]. The values for K_T and K_ε are dependent on the dopant species and concentration in the core of the fibre, but also to a lesser extent on the composition of the cladding and coating. Therefore, in the absence of strain, the temperature change can be defined as:

$$\Delta T_{measured} = -\frac{1}{K_T\nu}\Delta\nu_{T-DFOS} = C_T\Delta\nu_{T-DFOS} \quad (4)$$

Accordingly, the strain measurement can be compensated and calculated as follows:

$$\varepsilon_{measured} = -\frac{K_\varepsilon}{\nu}(\Delta\nu_{\varepsilon-DFOS} - \Delta\nu_{T-DFOS}) = C_\varepsilon(\Delta\nu_{\varepsilon-DFOS} - \Delta\nu_{T-DFOS}) \quad (5)$$

Assuming a scan centre wavelength of 1550 nm, the constants can be substituted in to yield the following temperature and strain conversion factors, respectively:

$$C_T = -0.801°C/GHz$$

$$C_\varepsilon = -6.67\varepsilon\mu\,/GHz$$

3 Methodology

3.1 Manufacturing of smart thermoplastic composite beam

The process used to produce the thermoplastic composite beams with integrated DOFS involved three steps, as shown in Figure 2.

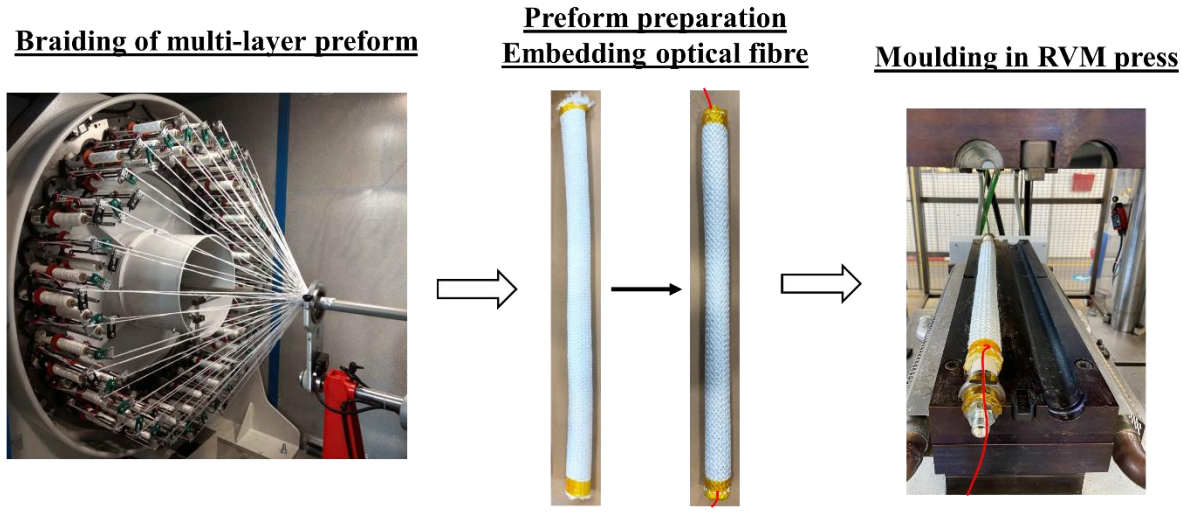

Figure 2: Key steps in manufacturing thermoplastic braided beams. Left: Braiding onto mandrel. Centre: Preparation for RVM and embedment of optical fibre. Right: Preform inside the press. The red line highlighted the insertion of ε-DOFS.

The process steps were described in detail below:

i. *Braiding and preform preparation*: A commingled material system procured from Coats plc composed of E-glass fibres and polyamide 6 (PA6) filaments was used to braid the preforms. The specification of the commingled material is listed in Table 2.

Table 2 Properties of commingled E-glass/PA6 material.

Property	Value
Linear weight	1650 g/km
Fibre weight fraction	72%
Theoretical fibre volume fraction	54%
E-glass density	2.54 g/ml
PA6 density	1.15 g/ml
PA6 melting point	221 °C
PA6 glass transition temperature	55 °C

The braiding of the circular hollow preforms was achieved at Composite Braiding Ltd using a 64-carier braiding machine. During the braiding process, the machine was operated at half-capacity, i.e. 32 carriers were employed to result in a 1×1 or diamond braid architecture. Three layers were overbraided on an acetal mandrel with an outer diameter of 25 mm. The machine parameters were set to achieve a target braid angle of 45° in all the braided layers. Following

the braiding process, the overbraided mandrels were transported to WMG for the moulding process.

ii. *Integration of optical fibre*: Preforms of approximately 480 mm long were extracted from the received mandrels. The preform length was back calculated based on the final beam length as well as the expected contraction during the moulding process. In order to secure the fibre architecture during handling as well as moulding, both ends of the preform were taped using a high temperature masking tape. The optical fibre employed in this study is a polyimide coated, low bend loss, single mode fibre, which was manually integrated between the outermost and second layer of the braided preform. This was performed by carefully removing the outer layer and laying the optical fibre upon the second layer. In order to protect the optical fibre, a 0.6 mm diameter Poly-Tetra-Fluoro-Ethylene (PTFE) coating was used in the ingress and egress portions. The coated portions were also secured to the ends of the second layer of the braid using masking tape to maintain orientation of the optical fibre. Finally, the outermost layer was carefully reinstated, and a silicone rubber bladder was put through the preform. Thus, there were no additional measures used to bond the optical fibre within the materials. Bespoke designed metallic end fittings were attached at both ends of the bladder that would enable internal pressurisation during the moulding process.

iii. *Moulding of braided preform*: The preforms were moulded using a novel bladder moulding technique called rapid variothermal moulding (RVM) developed previously by the authors [29]. The process used a hydraulic press integrated with a modern smart tooling concept developed by Surface Generation [30]. The tooling setup enabled rapid heating/cooling of the mould faces while maintaining thermal uniformity across the mould via localised thermal control. The moulding process involved the following steps:

   a. Preheating to 150 °C followed by preform insertion and mould closure.
   b. Application of 4 bar bladder pressure via an external hose connected to the end fittings.
   c. Temperature increase to a consolidation temperature of 240 °C (20 °C above the melting point of PA6).
   d. A pressure increase to 20 bar as the consolidation temperature was reached.
   e. Consolidation at 240 °C and 20 bar pressure for 15 minutes.
   f. Rapid but uniform cool down to below 185 °C, i.e. recrystallisation peak of PA6.
   g. Pressure release and demoulding of the consolidated preform at approximately 90 °C.

The produced tubular braided beam had an outer diameter of 35 mm. During the manufacturing process, the Optical Frequency Domain Reflectometry (OFDR) system from the LUNA Inc. (ODiSI-B model) was connected to the optical fibre and used to monitor the strain evolution in the composites. The total

strain from the interrogator was recorded and recalculated to account for the temperature compensation of fibre thermal output.

3.2 Interrupted mechanical tests

A static three-point flexural test were conducted using an Instron 3367 test machine with a 30 kN load cell in compression mode. The test setup was shown in Figure 3(a). The support span was 350 mm, which was consistent with those tested in previous studies by the authors [31,32]. The tests were performed in a loading-unloading interrupted scheme with a crosshead speed of 0.5 mm/min under displacement control. The purpose behind the interrupted test was to assess the ability of the DOFS for detecting damage in the tested composite beams with repetitive loads. In order to validate the measurement from DOFS, the acquired strain data was compared with the surface strain distribution of the braided beams captured using a three-dimensional digital image correlation (GOM 12 3D-DIC) system [31,32] in previous studies. The test specimen used in this work was manufactured using the same manufacturing parameters as the beams tested in the abovementioned previous studies. Therefore, it was deemed reasonable to assume identical mechanical behaviour for the specimen manufactured and tested in this work.

During the interrupted tests, a travelling microscope equipped with a digital camera was used to monitor the damage near the central point of load application on the beam, as shown in Figure 3(b). The test scheme included six loading-unloading cycles with progressively increasing maximum displacement, as indicated in Table 3. The scheme was based on observations from previously conducted continuous tests on identical beams [31,32]. The tests were finally stopped at a crosshead displacement of 13 mm as significant lateral movement was observed at the beam-support roller interfaces upon deflections beyond this.

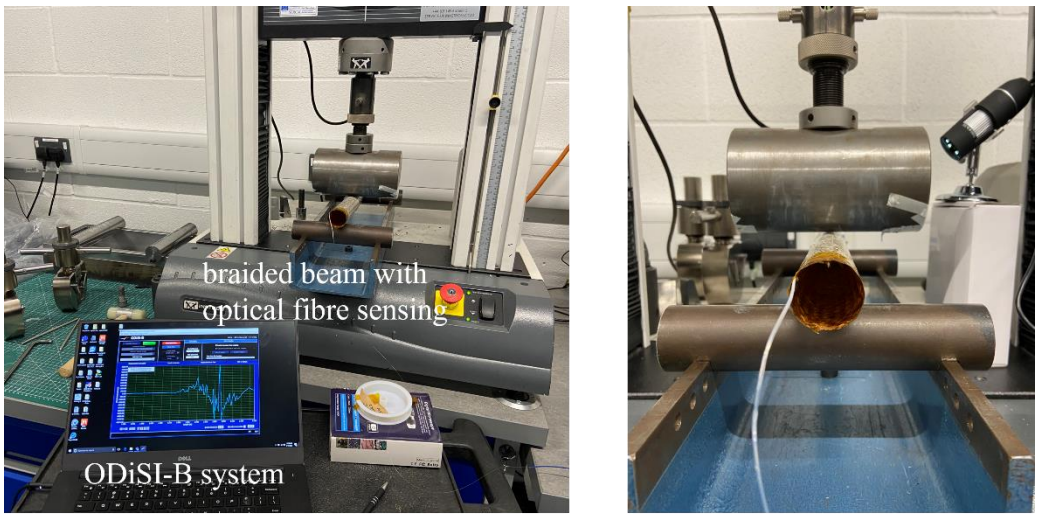

(a) (b)

Figure 3: (a) Three-point bending experimental set up with OFDR-bases interrogator for strain measurement, (b) traveling microscope used to measure damage during the interrupted test.

Table 3 Loading-unloading cycles of interrupted three-point bending test.

Loading cycle	Maximum displacement (mm)	Maximum load (N)
1	3.0	272.96
2	4.5	360.90
3	6.0	427.46
4	7.5	465.77
5	9.0	471.38
6	10.5	447.94

The DOFS was setup to acquire data at a rate of 1 Hz with a gauge length of 1.25 mm. Before starting any measurement, a reference OF tare was set up to erase any residual strains from the manufacturing process and measure solely the strain induced due to the application of mechanical load

3.3 Micro-CT

An X-Ray micro Computed Tomography (micro-CT) scan was performed at the Centre for Imaging, Metrology and Additive Technologies (CiMAT) at WMG, Warwick University to extract detailed information regarding the orientation and positioning of the optical fibre within the three-dimensional volume of the specimen, more generally, the quality of the embedment of the optical fibre sensor in the material. In this work, a TESCAN UniTOM XL system was used, while the post analysis was performed using commercially available software VGStudio Max 2.2.5. The obtained resolution of the X-Ray micro-CT scan was 35 µm and has been chosen as a compromise between a good image quality and being able to see as long as the optical fibre presents as the optical fibre might not be in the same visualised plane. The whole sample was scanned by merging 8 scans of region of interest. The other parameters used in the micro-CT scanning are listed in Table 4. The images obtained from the micro-CT scanning will be discussed in Section 4.2.

Table 4 Parameters used in the micro-CT scanning.

Exposure Voltage	80 kV
Exposure Power	35W
Exposure Time	75 msec
Voxel size	35 µm
No of Projections	1979
Frame per projections	3

4 Results and discussion

4.1 Strain monitoring during consolidation and cooling

Figure 4(a) displayed the temporal characteristics of the total strain shift along the embedded optical fibre length (measured from ε-DOFS) and the mould temperature (obtained from the Surface Generation user interface). Figure 4(b) showed the strain mapping along the embedded optical fibre length during

the consolidation and cooling process, with a clear distinction in the strain values across the phase transition (from liquid phase before recrystallisation to solid phase after recrystallisation). During the manufacturing process, the presence of rigid metallic end fittings at either end of the beam resulted in a physical constraint upon the optical fibre. This also resulted in the breakage of the optical fibre in close vicinity to the end fittings in several manufacturing trials. Therefore, in order to eliminate any artifacts introduced due to the end fittings, the strain data within approximately 150 mm from both the beam ends was omitted.

The temporal strain distribution was divided into four distinct stages (numbered I to IV) corresponding to the moulding process as described in Section 3.1. During the process timeline shown in Figure 4(a), the preform was always under a bladder pressure of at least 4 bar. Therefore, the strains represented and discussed here are a combination of thermal and mechanical strains. Moreover, for every stage, lengthwise strain data was also analysed. The standard deviation in the measured strain corresponding to a selection of temperature from different stages were listed in Table 5. Moreover, several snapshots depicting these variations were also shown with the temporal strain and temperature distribution in Figure 4(c).

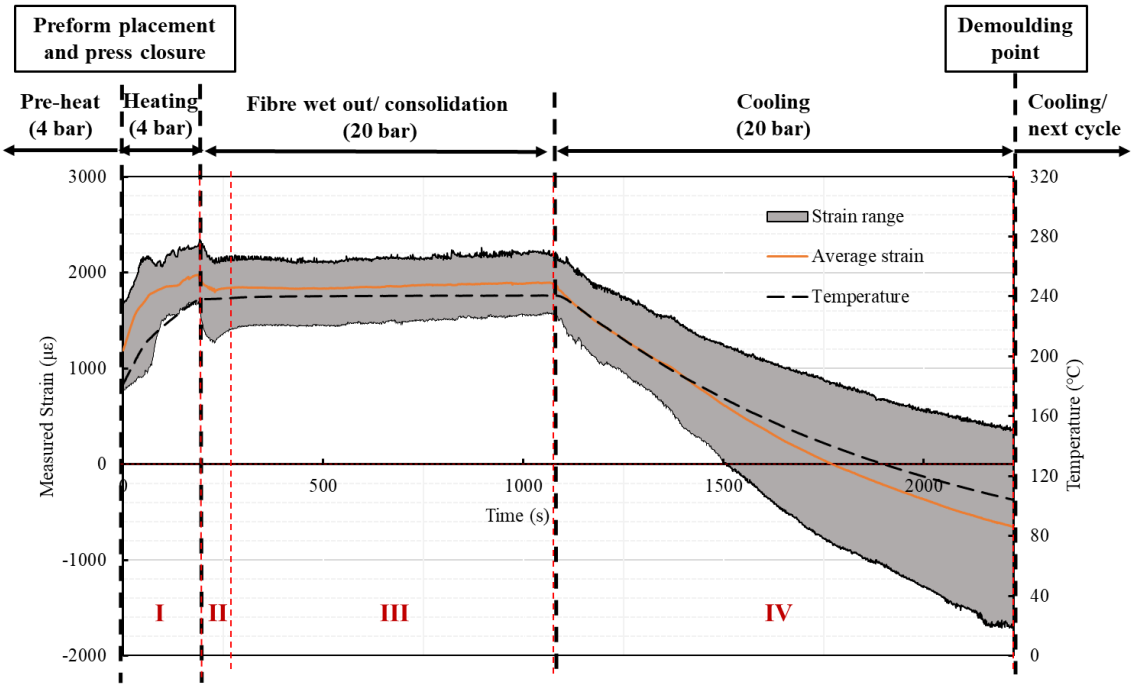

(a)

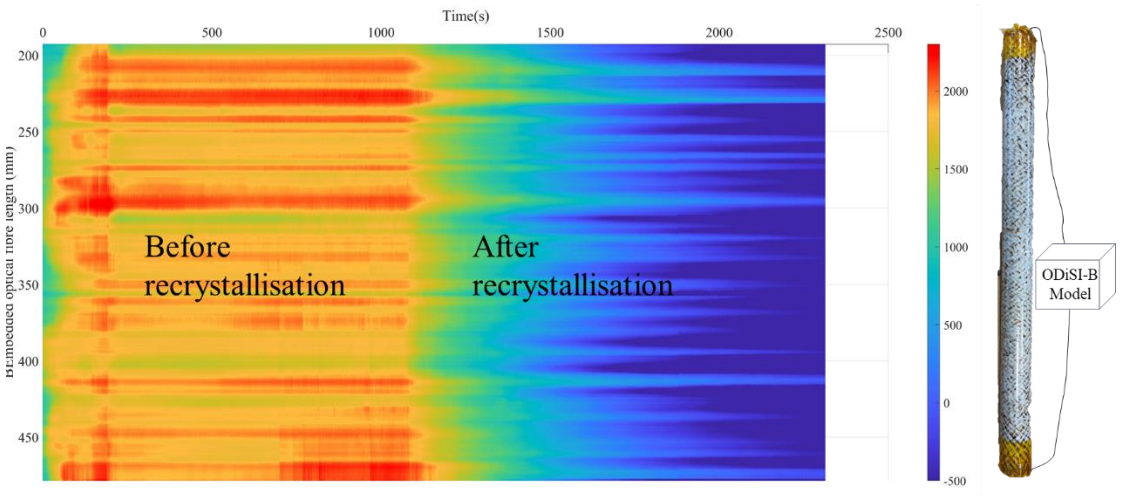

(b)

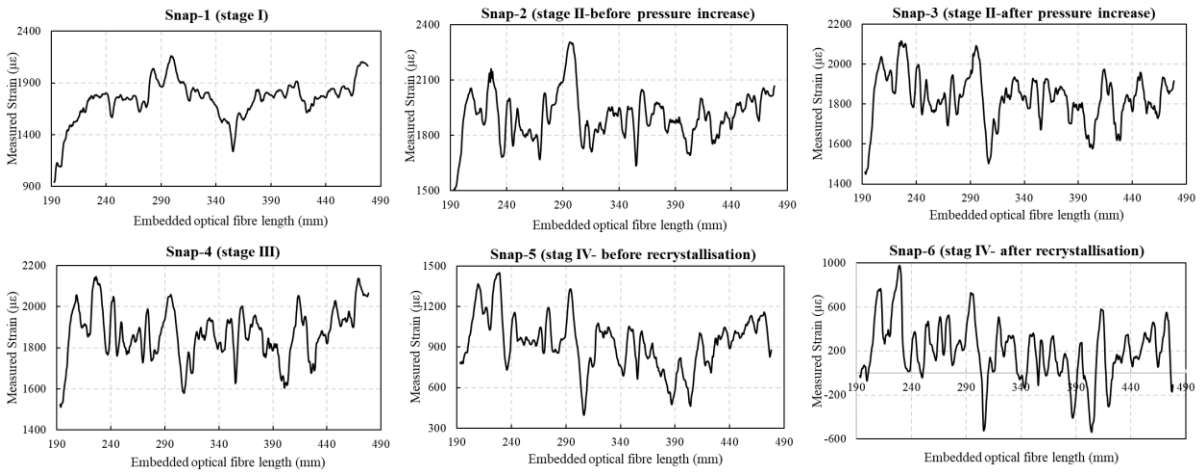

(c)

Figure 4: (a) The evolution of strain range along the embedded optical fibre length and the temperature measurement, (b) snapshots showing strain profiles along the length of the beam during different stages of the manufacturing process and (c) strain mapping along the embedded optical fibre length during the consolidation and cooling process.

Table 5 Standard deviation in the measured strain profiles during different stages of the manufacturing process.

S.No.	Temperature (°C)	Stage	Standard deviation (με)
1	170.98	I	191.380
2	223.49	II-before pressure application	129.279
3	240.08	II-after pressure application	121.232
4	240.53	III- during consolidation	126.744
5	201.73	IV- before recrystallisation	198.593
6	161.88	IV-post recrystallisation	264.951

The four stages of strain evolution are discussed below:

I. The mould ramped up to the consolidation temperature (240 °C) during the first stage. The temperature rise was primarily responsible for the observed positive strain. As shown in Table , the standard deviation during the initial phase of stage I were comparatively higher than the subsequent stages when the matrix was in a molten state. This is because before the PA6 melted, the material was in the form of bulkier commingled glass and PA6 tows. Therefore, the optical fibre underwent relatively severe undulations along its length compared to later stages after the melting of the PA6. This was schematically represented in Figure *5*.

II. In stage II, the PA6 was already above its melt temperature of 221 °C. Upon reaching the consolidation temperature of 240 °C, the pressure was increased from 4 to 20 bar. This increase in pressure was accompanied with a sharp drop in the strain values. This sharp drop was a result of the higher internal pressure upon the braided tows, which resulted in outwards squeeze of the molten PA6 from the tows, thus compressing the tows in the thickness direction. This phenomenon was also depicted in Figure *5*. As shown in the figure, the decrease in the tow thickness reduced the undulations in the optical fibre, thus resulting in a decrease in tension along their length.

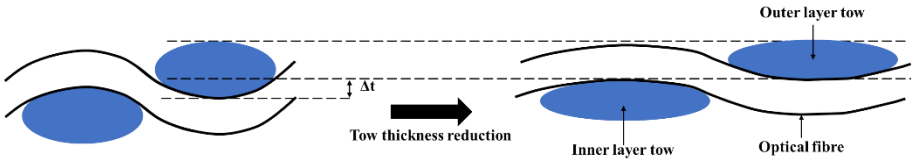

Figure 5: Schematic representation of decrease in optical fibre undulation upon reduction in braided tow thickness.

III. During stage III, a temperature of 240 °C was maintained for 15 minutes, The strain values showed a stable trend during this regime with a constant peak to peak strain value as listed in Table .

IV. The cooling began in this stage and the strains started to decrease with the temperature. It could be observed from Table that the deviation in the strain values increased with decreasing temperature. The rise was particularly higher beyond the recrystallisation temperature of 185 °C, i.e., the point at which the matrix solidified. This effect was further elaborated in Figure 6, which shows the lengthwise strain evolution during the cooling phase of the process.

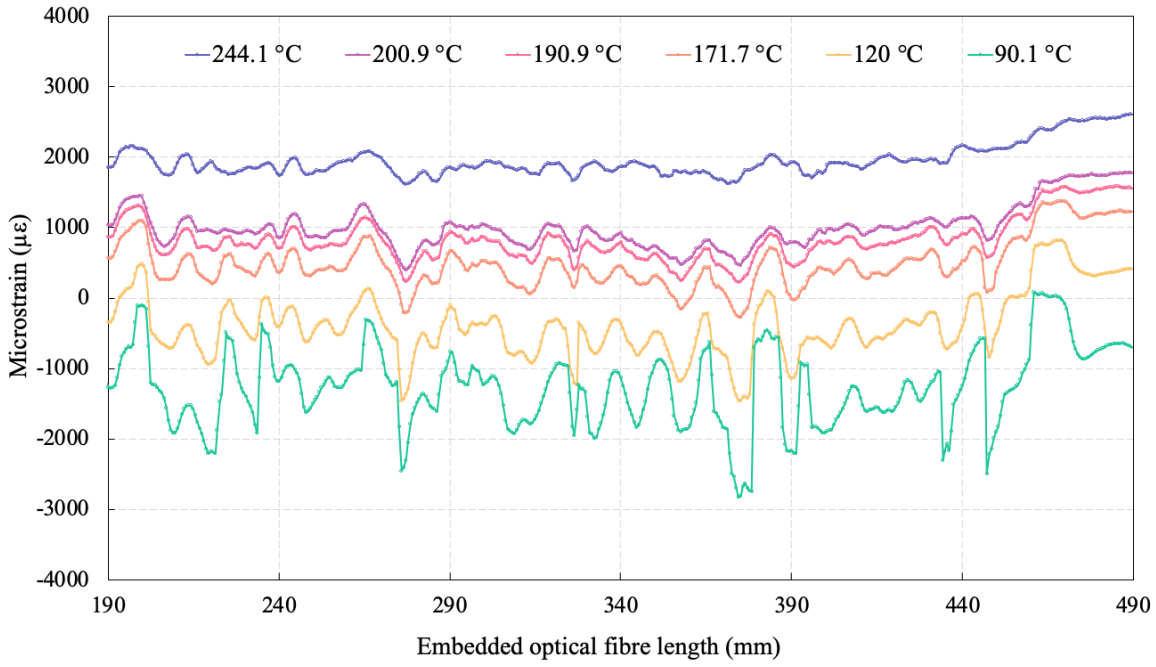

Figure 6: Temporal evolution in measured strain along the length of the embedded optical fibre.

This rise could be attributed to two competing mechanisms. Firstly, as reported for the bladder moulding of the considered material system previously [32], the glass fibres on the outer surface showed waviness. This distortion was speculated to be caused by the compressive residual strains induced during the cooling phase of the process. Similar results were also reported in [33]. The optical fibre would also experience comparative residual strains in along its axis and hence undergo waviness. A Micro-CT scanning image of the consolidated beam, as shown in Figure 7, confirmed the presence of waviness in the optical fibre. Therefore, the resulting variability in the orientation of the optical fibre would cause the measured strain to deviate from the braided composite beam's axis and therefore induce a variation in the results.

Secondly, during the post-consolidation, the braided composite had a periodic inhomogeneous material system, which is inherent to all textile composites. In the context of thermal strains, this inhomogeneity manifested in the form of variable thermal expansion coefficient, i.e., the optical fibre was subjected to periodically repetitive variations in thermal expansion contraction as per the local thermal properties.

Eventually, a mean compressive residual strain of 479 με was recorded before demoulding the beam at approximately 90 °C.

4.2 Profile of DOFS in braided composites

As the DOFS was embedded in braided composites, the differences in compaction of the yarns/tows during resin consolidation may lead to different sensor profiles. Therefore, micro-CT was used as a tool to help interpret the position check of the sensor profile. **Error! Reference source not found.** showed the non-planar view of two sections extracted from the 3D rendering. Three images were presented: the

first two images (*a*, *b*) showed the embedded DOFS between the layers of braided composites, (*c*) is an enlarged image of part at the termination of the composite beam where the fibre was encapsulated within a protective PTFE coating and (*d*) is the side view of the enlarged embedded optical fibre within composites. All the images indicated negligible control over the orientation of the optical fibre within the braided composite. As discussed in Section 4.1, there were multiple phenomenons that could result in an undulating/wavy profile of the optical fibre. It was also observed in [24] where the OF was embedded between woven-fabric (90,0) layers and a shift of OF profile between the adjacent woven plies was observed as well as some differences in the spectrum of the OF reflected signal (e.g., peak splitting and shouldering). In reference [10], micro-braiding of the DOFS with a glass tow was attempted for improved handling and mechanical properties of the OFs, however, the micro-braiding did not affect the sensitivity. Nevertheless, it was found in this study that the strain measurements were comparable and reasonable for the investigation, however, it would also be interesting to introduce the micro-CT images to identify the OF profile to understand the standing switch during the manufacturing. As the signals did not show spikes despite waviness, it was believed that the orientation was not crucial for the purpose of SHM.

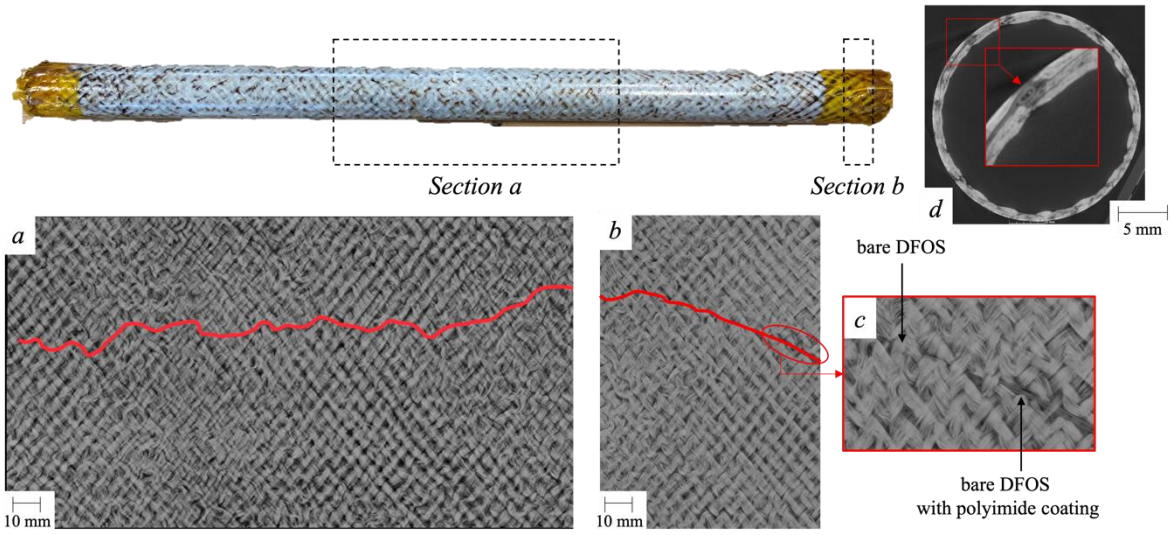

Figure 7: Non-planar view of two sections (*a*, *b*) taken along the beam embedded with DOFS. The highlighted red line indicated the locations of the optical fibre; (c) is the enlarged image taken from image *b* to show the termination layout of the bare DFOS and bare DFOS with PTFE coating; (d) is the side view of the enlarged embedded optical fibre within composites

4.3 Structural health monitoring during three-point flexure test

The load-midspan displacement curve obtained from interrupted tests was presented in Figure 8. Every loading cycle (LC) was composed of two phases: a rising load phase (RL) and a decreasing load phase (DL). In the initial load cycle, i.e. LC1, the load-displacement data showed a linear trend during the RL phase. However, during the DL phase, an offset relative to the RL phase was observed. During the RL

phase of LC2, the load replicated the linear curve obtained from RL during LC1. This overlap in the load-displacement curve indicated that the material retained its stiffness and therefore did not undergo any damage during LC1. The observed offset after load removal in DL phase (of LC1) could have occurred due to a rate-dependent relaxation phenomenon, however, further works needed to confirm this speculation. After moving beyond the load threshold of LC1, there was observable non-linearity in the LC2 curve. In addition, upon the end of the DL phase in LC2, the positional offset from the initial point increased further. In the next loading cycle LC3, the RL phase showed a decrease in stiffness compared with LC1 and LC2. These observations indicated that the non-linearity observed in LC3 could be a sign of microcracks damage initiation (< 50 μm). As expected, the stiffness degradation and increase in zero-load offset were observed to rise in the further load cycles (LC3 to LC4). The failure load was kept increasing with the gradual reduction on the material stiffness, which might be related to the generation of fictitious cracks (> 50 μm). Finally, when the beam resistance was maximum with the force of 471.3 N (LC5), gradual degradation with a rise in deflection continued as the localised fictitious cracks propagated and the fibre was yielding, with a comparatively reduced peak load in LC6.

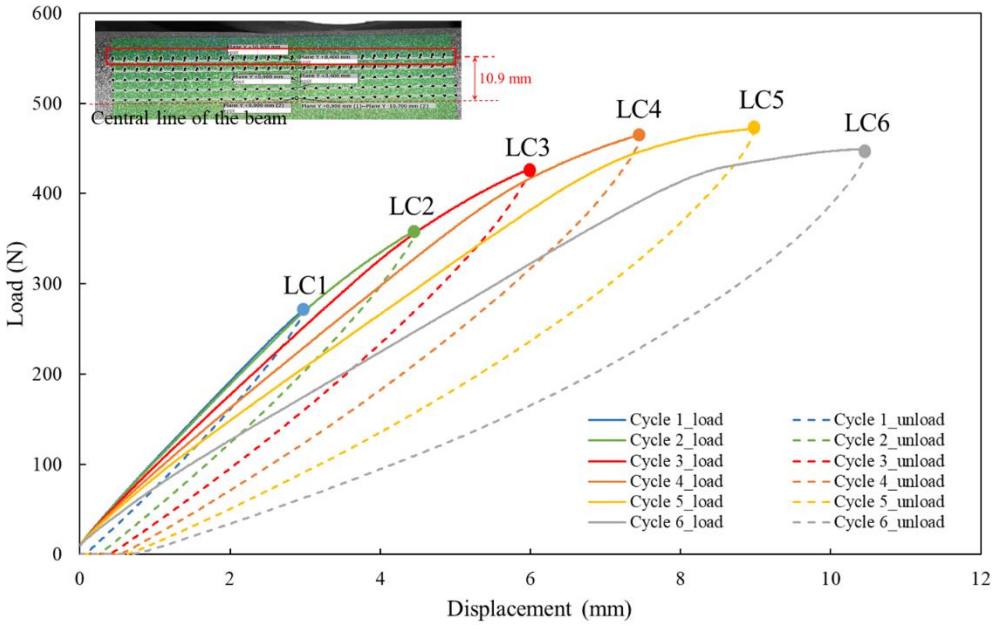

Figure 8: Load-displacement curve of the braided composite beam during interrupted quasi-static test. The load cycles (LCs) in interrupted tests are marked. The left corner image indicates the virtual measurement line of DIC.

Figure 9 (left) showed the horizontal strain distribution measured using the DIC along the central portion (depth-wise). Despite the minute undulations, the CT images from Figure 7 indicated that the fibre was relatively straight in the central portion of the beam, where DIC strain measurements were performed. Hence, this comparison is suitable. For DIC, the virtual measurement lines (indicated in Figure 9, positioned at 10.9 mm above the centre line), which was at the same height as the location of DOFS were prepared. The comparisons between DIC data and DOFS measurements at the

displacements corresponding to maximum displacements in LC1 to LC3 were used for validation. For LC1 to LC3, a reasonable correlation was observed between the DIC and DOFS data. This is because, despite the interrupted nature of the performed tests in this work, the beam did not undergo any damage in LC1 and hence the LC2 deformation was identical to that of a beam tested continuously. Despite the stiffness drop observed in LC3, the strain data from DIC and DOFS showed similar trends, with an observable positive strain developing in the region corresponding to the load application point. As noted in references [31,32], this was likely due to the localised loading underneath the roller that resulted in a deviation from the strain profile observed for ideal three-point flexure.

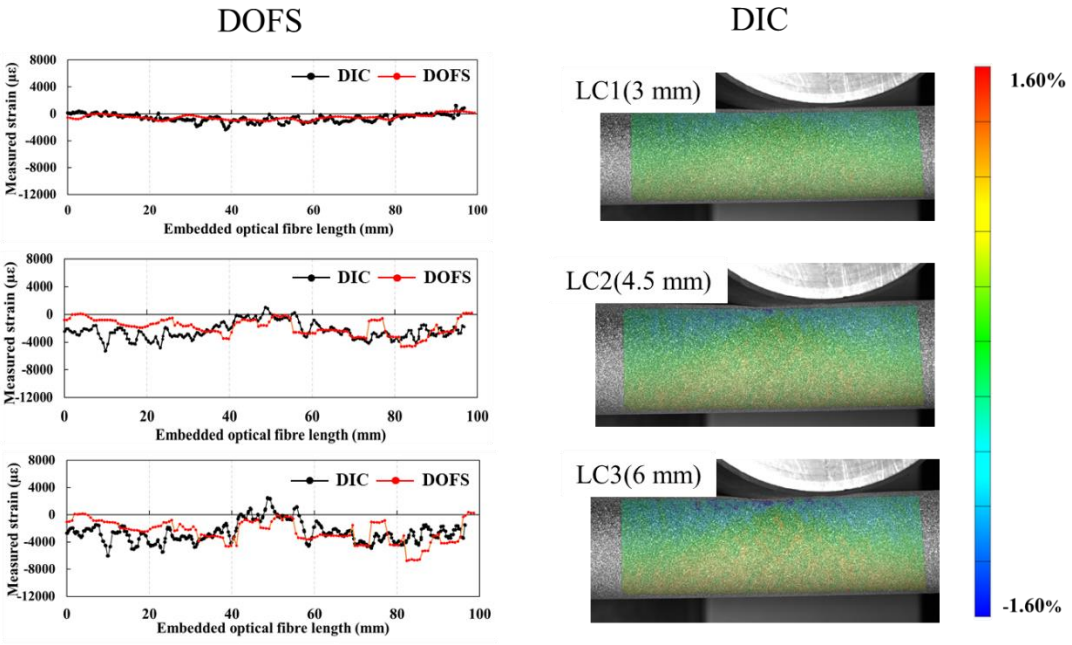

Figure 9: Strains measured along the embedded optical fibre length under cycle 1 to cycle 3 (left) compared with DIC data (right) for validation only, the black and red lines are for DIC and DFDS, respectively; the colour scale for DIC is presented.

Figure 10(a) showed the strain profiles taken at the maximum displacement points of each load cycle along the embedded optical fibre length. The increase in the strain peak from LC1 to LC3 was constant until a significant strain change occurred at LC4. At LC4, localised peaks around the middle position were visible from DOFS: this abrupt change could be an indication of significant local damage within fibres. At LC5, some dropout points started to appear at around crack locations, which was caused by the spectral shift calculation algorithm due to the low correlation with the reference spectrum [17]. This phenomenon of miscalculated spike point was increasing due to the rapid variation in the strain gradient in composites for a 1.25 mm gage length in the ODiSI-B system, which was also observed in [10,17]. During the loading and unloading associated with LC1 to LC5, the strain data recorded by DOFS was able to return to the initial starting point during the unloading process. However, for LC6, the strain configuration measurement indicated the breakage of the optical fibre so the signal could not return. As

the strain profile showed an undulating profile, a Fast Fourier Transform (FFT) study was conducted to convert the original signal to a representation in a hypothetical frequency domain in order to further differentiate between the strain profiles pertaining to different cycles. The normalised FFT data, shown in Figure 10 (b) and Figure 10(c), indicated no pattern shift in the first three LCs. However, a significant variation was observed for LC4, which could be associated with a significant damage initiation. In order to validate this, surface pictures of the loaded region of the beam captured using the travelling microscope at 40X magnification were observed. These pictures were shown in Figure 11. The pictures were taken after the unloading process of each cycle. While there was no visible sign of surface cracks till LC3, a dominant crack and a side crack were suddenly observed since LC4. These cracks were further observed to propagate during LC5. Based on the position with respect to the embedded length of the DOFS, it was speculated that the dominant crack propagated to the DOFS location during LC6, which resulted in the breakage of DOFS. Therefore, the post observation results and the correlations between visible damage and a clear change in the strain signal after FFT processing have proved that the embedded DOFS was sensitive to the growth of damage to a certain length in the composites and could be implemented for structural health monitoring. Although it is difficult to locate the damage initiation second due to the lack of efficient damage observation methodology and a schematic un-supervised data analysis of the strain data, the results were still significant as it could capture the instant when considerable damage exist (i.e., approximately 5 mm) for inspection check upon damage tolerance strategy.

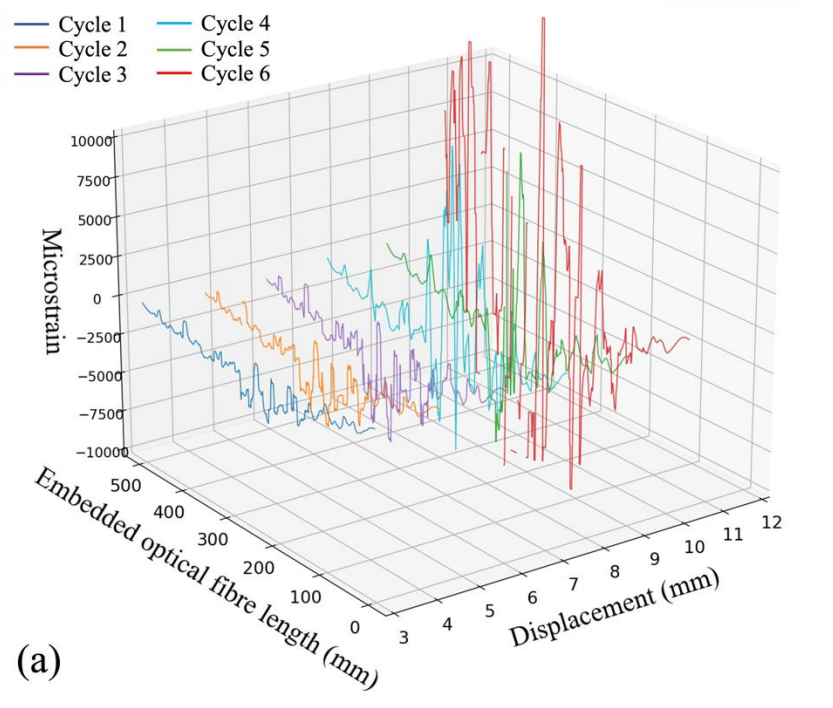

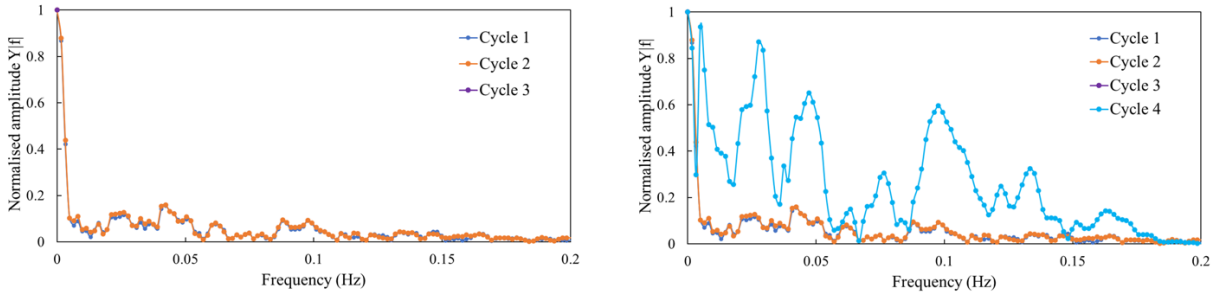

(b) (c)

Figure 10: (a) Strain profiles along the embedded optical fibre length at the maximum displacement points of different load cycles, (b) The normalised FFT study of LC1 to LC3 and (c) LC1 to LC4.

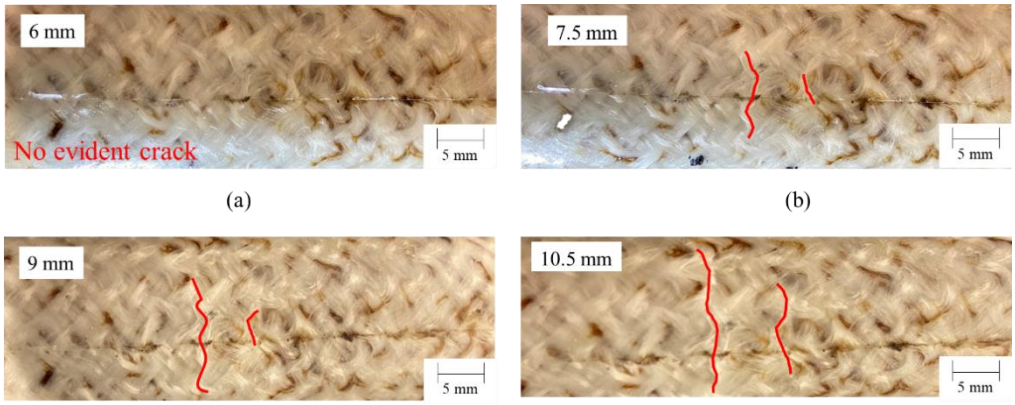

(a) (b)

(c) (d)

Figure 11: Damage observation after the unloading process of different cycles (a) cycle 3 (6 mm), (b) cycle 4 (7.5 mm), (c) cycle 5 (9 mm), (d) cycle 6 (10.5 mm) taken by 40× travelling microscope. The crack was marked by the red line.

The above results indicated that despite the lack of control over the optical fibre's orientation, by processing and comparing the acquired strain values over time allowed for identification of damage. This showed that the crude nature of the method adopted to embedded optical fibre within the composite did not affect its ability to monitor damage and successfully performed the expected role on structural health monitoring. Thus, without adding significant cost or time to the composite manufacturing process, the results demonstrated a simple yet effective route towards SHM of braided composite structures.

5 Conclusions

This paper demonstrated the integration of DOFS into a braided thermoplastic composite component. The optical fibre was manually embedded between the two outermost layers of a braided composite beam such that the manufacturing process was barely disrupted. The ODiSI-B system coupled with the embedded DOFS was shown to successfully measure strains during the consolidation process as well

during mechanical testing in real-time. The position of OF profile was further interpreted by a micro-CT scanning to define a reliable embedding.

The strain measured during the moulding process was correlated with the thermal and mechanical changed that occurred in the material. The measured strain of the braided material was directly correlated with the temperature trend at every stage of the consolidation and cooling process, shifting from tensile strain to compressive strain during the cooling due to the stress relief of the resin. The phase change from a molten state to semi-crystalline could be observed from strain measurement. Following the demoulding at 90 °C, the residual strain was measured, which was difficult and expensive to evaluate from the traditional approaches. The observed patterns in the strain measurements along the embedded optical fibre length during the cooling stage showed an undulating trend, which increased with reducing temperature. This was attributed to two phenomenons: (i) waviness caused in the optical fibre as a consequence of thermal contraction or lack of orientation control during the embedding process or (ii) the periodic braid architecture of the fully consolidated part with a varying thermal property along the length of the beam.

The micro-CT scans of the consolidated braided beam revealed a lack of consistency in the optical fibre's orientation. Moreover, they also revealed the presence of waviness in the embedded optical fibre, thus validating its effect on the observed increase in the undulating strain measurements. Further research on integrating the DOFS during braiding as tri-axial preforms for strain measurement would be significant.

The SHM capability of the DOFS was assessed by performing three-point flexure tests on the manufactured beam. The validity of the DOFS's strain measurement was confirmed through a reasonable correlation between the obtained strain values and surface strain data from DIC measurement. In order to track the damage of the beam, a travelling microscope was used to record pictures of the loaded region after each unloading stage. The obtained strain data was further processed using a Fast Fourier Transform. It was found that an abrupt shift in the processed data had a direct match with a significant damage observed via the captured surface pictures, thus proving the effectiveness of the DOFS in indicating damage for inspection check.

The results proved that the approach used to integrate the optical fibre without any specific mechanism to ensure its orientation (hence cause minimum disruption to the manufacturing process) was a valid method for performing structural health monitoring. Despite the lack of orientation control and induced imperfections in the optical fibre during the moulding process, the comparative analysis of the strain signal after being processed via FFT showed a significant shift corresponding to the load cycles in which visible damage was observed.

Further work aimed at repeating the experiments with reduced gap between consecutive load cycles would establish the absolute limit of the optical fibre's damage detection ability. Moreover, in-situ NDT

(i.e., Computed Tomography during manufacturing as well as mechanical testing) could provide further insights into the changes occurring in the composite and correlate them with strain measurements for improving the capability of optical fibre to assess manufacturing defects as well as damage initiation in real-life structures. Moreover, further research based on data-driven models is also recommended as a means of creating more efficient methodologies to produce reliable un-supervised damage estimation.

6 Acknowledgements

The researchers would like to acknowledge the support of the Catapult funding's (Grant reference: 160080 CORE HVMC(WMG)) to Dr Yiding Liu and Lab X-ray 659 CT (Grant reference: EP/T02593X/1) from EPSRC National Research Facility to Prof Mark Williams, which made the completion of this project possible. Authors also appreciate the support of LUNA and technical suggestions of Mr Ian Shannan.

7 Data availability statement

The datasets generated during and/or analysed during the current study are available from the corresponding author on reasonable request.

References

[1] McIlhagger A, Archer E, McIlhagger R. Manufacturing processes for composite materials and components for aerospace applications. Polym. Compos. Aerosp. Ind., Elsevier Inc.; 2015, p. 53–75. doi:10.1016/B978-0-85709-523-7.00003-7.

[2] Giurgiutiu V. Chapter 5-Damage and failure of aerospace composites. Struct Heal Monit Aerosp Compos 2016:125–75.

[3] Liu Y, Zhang X, Lemanski S, Yazdani H, Ayre D. Finite element study on the static and fatigue behaviour of wide single lap bonded joints with semi-circular defect. Int. Conf. Compos. Struct., vol. 573, 2018, p. 1–23.

[4] Liu Y, Lemanski S, Zhang X, Ayre D, Yazdani H. A finite element study of fatigue crack propagation in single lap bonded joints with process-induced disbond. Int J Adhes Adhes n.d.:1–18.

[5] Kessler SS. Certifying a structural health monitoring system: Characterizing durability, reliability and longevity. Proc. 1st Int. Forum Integr. Syst. Heal. Eng. Manag. Aerospace, Napa, CA, 2005, p. 7–10.

[6] Jardine AKS, Lin D, Banjevic D. A review on machinery diagnostics and prognostics implementing condition-based maintenance. Mech Syst Signal Process 2006;20:1483–510. doi:10.1016/j.ymssp.2005.09.012.

[7] Güemes A, Fernández-López A, Díaz-Maroto PF, Lozano A, Sierra-Perez J. Structural health monitoring in composite structures by fiber-optic sensors. Sensors (Switzerland) 2018;18:1–11. doi:10.3390/s18041094.

[8] Pan XW, Liang DK, Li D. Optical fiber sensor layer embedded in smart composite material and structure. Smart Mater Struct 2006;15:1231–4. doi:10.1088/0964-1726/15/5/010.

[9] Rufai O, Gautam M, Potluri P, Gresil M. Optimisation of optical fibre using micro-braiding for structural health monitoring. J Intell Mater Syst Struct 2019;30:171–85. doi:10.1177/1045389X18810805.

[10] Rufai O, Chandarana N, Gautam M, Potluri P, Gresil M. Cure monitoring and structural health monitoring of composites using micro-braided distributed optical fibre. Compos Struct 2020;254:112861. doi:10.1016/j.compstruct.2020.112861.

[11] Mulle M, Wafai H, Yudhanto A, Lubineau G, Yaldiz R, Schijve W, et al. Process monitoring of glass reinforced polypropylene laminates using fiber Bragg gratings. Compos Sci Technol 2016;123:143–50. doi:10.1016/j.compscitech.2015.12.020.

[12] Sorensen L, Gmür T, Botsis J. Residual strain development in an AS4/PPS thermoplastic composite measured using fibre Bragg grating sensors. Compos Part A Appl Sci Manuf 2006;37:270–81. doi:10.1016/j.compositesa.2005.02.016.

[13] Arhant M, Meek N, Penumadu & D, Davies P, Garg & N. Residual Strains using Integrated Continuous Fiber Optic Sensing in Thermoplastic Composites and Structural Health Monitoring. Exp Mech 2018;58:167–76. doi:10.1007/s11340-017-0339-2.

[14] Huang C, Bao X, Zeng X, Arcand A, Lee-Sullivan P. Simultaneous temperature and strain monitoring of composite cure using a Brillouin-scattering-based distributed fiber optic sensor. Smart Struct. Mater. 2001 Sens. Phenom. Meas. Instrum. Smart Struct. Mater., vol. 4328, SPIE; 2001, p. 70. doi:10.1117/12.435544.

[15] De Baere I, Luyckx G, Voet E, Van Paepegem W, Degrieck J. On the feasibility of optical fibre sensors for strain monitoring in thermoplastic composites under fatigue loading conditions. Opt Lasers Eng 2009;47:403–11. doi:10.1016/j.optlaseng.2008.01.001.

[16] Califano A, Chandarana N, Grassia L, D'amore A, Soutis C. Damage Detection in Composites By Artificial Neural Networks Trained By Using in Situ Distributed Strains n.d. doi:10.1007/s10443-020-09829-z.

[17] Sawicki B, Bassil A, Brühwiler E, Chapeleau X, Leduc D. Detection and measurement of matrix discontinuities in uhpfrc by means of distributed fiber optics sensing. Sensors (Switzerland) 2020;20:1–21. doi:10.3390/s20143883.

[18] Lau KT, Chan CC, Zhou LM, Jin W. Strain monitoring in composite-strengthened concrete structures using optical fibre sensors. Compos Part B Eng 2001;32:33–45. doi:10.1016/S1359-8368(00)00044-5.

[19] Ryu CY, Lee JR, Kim CG, Hong CS. Buckling behavior monitoring of a composite wing box using multiplexed and multi-channeled built-in fiber Bragg grating strain sensors. NDT E Int 2008;41:534–43. doi:10.1016/j.ndteint.2008.05.001.

[20] Minakuchi S, Takeda N, Takeda SI, Nagao Y, Franceschetti A, Liu X. Life cycle monitoring of large-scale CFRP VARTM structure by fiber-optic-based distributed sensing. Compos Part A Appl Sci Manuf 2011;42:669–76. doi:10.1016/j.compositesa.2011.02.006.

[21] Mason H. Collins Aerospace invests in braiding technology for Banbury, U.K. facility n.d.

[22] Kelkar AD, Whitcomb JD. Characterization and structural behavior of braided composites. 2009.

[23] Arold B, Gessler A, Metzner C, Birkefeld K. Braiding processes for composites manufacture. Adv. Compos. Manuf. Process Des., Elsevier; 2015, p. 3–26.

[24] Chiesura G, Luyckx G, Voet E, Lammens N, van Paepegem W, Degrieck J, et al. A Micro-Computed tomography technique to study the quality of fibre optics embedded in composite materials. Sensors (Switzerland) 2015;15:10852–71. doi:10.3390/s150510852.

[25] Lee B. Review of the present status of optical fiber sensors. Opt Fiber Technol 2003;9:57–79. doi:10.1016/S1068-5200(02)00527-8.

[26] Bao X, Chen L. Recent progress in distributed fiber optic sensors. Sensor 2012;12:8601–39. doi:10.3390/s120708601.

[27] Kreger ST, Gifford DK, Froggatt ME, Soller BJ, Wolfe MS. High resolution distributed strain or temperature measurements in single- and multi-mode fiber using swept-wavelength interferometry. Opt InfoBase Conf Pap 2006. doi:10.1364/ofs.2006.the42.

[28] Froggatt M, Moore J. High-spatial-resolution distributed strain measurement in optical fiber with Rayleigh scatter. Appl Opt 1998;37:1735–40. doi:10.1364/AO.37.001735.

[29] Singh A, Reynolds N, Carnegie CR, Micallef C, Keating EM, Winnett J, et al. A novel route for volume manufacturing of hollow braided composite beam structures. Adv Manuf Polym Compos Sci 2019;5:224–9. doi:10.1080/20550340.2019.1680514.

[30] Surface Generation n.d.

[31] Singh A, Reynolds N, Keating EM, Barnett AE, Barbour SK, Hughes DJ. Three-point flexural performance of tailor-braided thermoplastic composite beam structures. Compos Struct 2021;260. doi:10.1016/j.compstruct.2020.113521.

[32] Singh A, Reynolds N, Keating EM, Barnett AE, Barbour SK, Hughes DJ. The effect of braid angle on the flexural performance of structural braided thermoplastic composite beams. Compos Struct 2020:113314. doi:https://doi.org/10.1016/j.compstruct.2020.113314.

[33] Krämer ETM, Grouve WJB, Warnet LL, Koussios S, Akkerman R. Tool-ply interaction in the formation of waviness during C/PEEK consolidation. Compos Part A Appl Sci Manuf 2021;144:106327.